1            *Title*

2            **Degenerating *Drosophila* Larval Epidermal Cells Drive Thorax Closure**

3            *Running title*

4            Larval epidermis drives *Drosophila* thorax closure

5            *Keywords*

6            Thorax closure, Larval epidermis, Organogenesis, *Drosophila*

7            *Authors*

8            Thamarailingam Athilingam[1, 2, 3], Saurabh Singh Parihar[1, 2], Rachita Bhattacharya[1],

9            Mohd. Suhail Rizvi[1, 4], Amit Kumar[1,5] and Pradip Sinha[1,]*

10

11            [1]Department of Biological Sciences and Bioengineering

12            Indian Institute of Technology Kanpur, India, 208016

13            [2]These authors contributed equally

14            [3]Current address: Mechanobiology Institute, National University of Singapore

15            5A Engineering Drive 1, Singapore 117411

16            mbita@nus.edu.sg

17

18            [4]Current address: Indian Institute of Technology Hyderabad, India 502285

19            suhailr@bme.iith.ac.in

20

21            [5]Current address: Albert Einstein College of Medicine, 1300 Morris Park Avenue

22            Bronx, New York

23            amit.kumar@einsteinmed.org

24

25            *Author for correspondence:

26            pradips@iitk.ac.in

**Abstract**

Adult thorax formation in *Drosophila* begins during pre-pupal development by fusion of its two contralateral progenitor halves, the heminotal epithelia (HE). HEs migrate and replace an underlying cell layer of thoracic larval epidermal cells (LECs) during a morphogenetic process called thorax closure. The LEC layer has so far been proposed to be a passive substrate over which HEs migrate before their zipping. By contrast, here we show that the pull forces generated within the LEC layer drive HE migration. During thorax closure, the LECs display actomyosin-mediated contraction, via enrichment of non-muscle myosin-II and actin, besides squamous-to-pseudostratified columnar epithelial transition and tissue shrinkage. This shrinkage of the LEC layer is further accompanied by cell extrusion and death, that prevent overcrowding of LECs, thereby promoting further shrinkage. The pull forces thus generated by the shrinking LEC layer are then relayed to the HEs by their mutual adhesions via βPS1 (Mys) and αPS3 (Scb) integrins. Suppression of cell death in the LEC layer by a gain of p35 leads to cell overcrowding, which impedes HE migration and zipping. Further, knockdown of *sqh*, the light chain of non-muscle myosin II, in LECs or integrins (*mys* or *scb*) in either the LEC layer or in the HEs, or both abrogate thorax closure. Mathematical modeling also reveals the biophysical underpinnings of the forces that drive this tissue closure process wherein a degenerating LEC layer mediates its succession by the future adult primodia. These essential principles of thorax closure appear ancient in origin and recur in multiple morphogenetic contexts and tissue repair.

**Introduction**

During larval-pupal molt in holometabolous insects, a high ecdysone hormone titer triggers the replacement of larval structures by their adult primordia (for a recent review, see (Truman and Riddiford, 2019)). Thorax closure in *Drosophila* exemplifies one such morphogenetic event where larval epidermal cells (LECs) of the three thoracic body segments are replaced by their corresponding adult primordia. Adult thorax (or notum) is formed from three paired imaginal progenitors: namely, dorsal prothoracic (humeral) discs, proximal cells of the mesothoracic wing discs, and the metathoracic haltere imaginal discs (for review, see (Beira and Paro, 2016; Fristrom and Fristrom, 1993)). These bilateral precursors of the adult thorax, following their eversion (Pastor-Pareja et al., 2004), undergo fusion with each other to form two contralateral

56    heminotal epithelia (HE), one each on the left and the right thoracic region of the prepupa.

57    Thorax closure ensues (Fristrom and Fristrom, 1993) when these two opposing contralateral HEs

58    migrate, replacing the LEC layer and zip at the future midline of the adult body: a culmination of

59    an elegant process of epithelial tissue closure (see Figure S1A) (Agnès et al., 1999; Kumar et al.,

60    2020; Martín-Blanco et al., 2000; Usui and Simpson, 2000; Zeitlinger and Bohmann, 1999).

61    Historically, studies on thorax closure (Agnès et al., 1999; Martín-Blanco et al., 2000; Usui and

62    Simpson, 2000; Zeitlinger and Bohmann, 1999) closely followed the leads obtained from another

63    epithelial tissue closure event in *Drosophila*: namely, embryonic dorsal closure (DC) (for review,

64    see (Belacortu and Paricio, 2011)). Like in thorax closure, during DC too, two lateral embryonic

65    epidermal cell sheets converge dorsally, replacing an extra-embryonic flattened epithelial cell

66    layer, the amnioserosa (for recent reviews, see (Hayes and Solon, 2017; Kiehart et al., 2017)).

67    Anatomical parallels could be drawn between the embryonic amnioserosa and the thoracic LEC

68    layer as both degenerate and are replaced during their respective tissue closure events. Likewise,

69    lateral embryonic epidermis and pre-pupal HEs represent the cell layers that migrate during DC

70    and thorax closure, respectively. The leading edges (LEs) of the lateral embryonic epidermis

71    have been proposed to mediate DC based on their supracellular actin cables via their purse-

72    string-like contractions (Kiehart et al., 2000), while actin-rich filopodial projections from the

73    LEs contribute to their zipping (Jacinto et al., 2002). Given these precedences in DC, previous

74    studies in thorax closure also explored the LEs of HEs as potent hubs of mechano-regulation and

75    cell signaling (for review see, (Belacortu and Paricio, 2011; Harden, 2002)). Indeed, it was seen

76    that perturbations in signaling pathways such as JNK, D-Fos, or Dpp in the LEs, affect thorax

77    closure, reminiscent of similar outcomes in DC (for review, see (Belacortu and Paricio, 2011;

78    Harden, 2002; Martín-Blanco and Knust, 2001)). Further, LEs of HEs also displayed actin-rich

79    filopodia (Agnès et al., 1999; Martín-Blanco et al., 2000; Pastor-Pareja et al., 2004; Usui and

80    Simpson, 2000; Zeitlinger and Bohmann, 1999), that are known to display reversible contacts

81    with substratum in various morphogenetic contexts (Parsons et al., 2010). It was therefore

82    proposed that contralateral HEs crawl over the LEC layer, wherein the underlying LECs are left

83    'below and behind and eventually delaminate from the edges'(Martín-Blanco et al., 2000). In

84    essence, these interpretations of thorax closure present the thoracic LEC layer as a scaffold over

85    which HEs migrate (see Figure 6 in (Martín-Blanco et al., 2000)). Indeed, somewhat comparable

86    roles LEs play in other organisms, such as gastrulation in sea urchin embryo (Gustafson, 1963),

87    ventral enclosure in *C. elegans* (Williams-Masson et al., 1997), or closure of epithelial gaps

88    during wound healing (Martin, 1997; Martin and Lewis, 1992) presented a framework wherein

89    LEs of migrating HEs appeared as the drivers of thorax closure.

90    Subsequent studies on DC, however, led to a substantial revision in the understanding of its

91    mechanism wherein amnioserosa—rather than the LEs of the lateral embryonic epidermis—was

92    shown to be the principal source of forces for tissue closure. For instance, amnioserosa shrinks

93    by apoptosis (Toyama et al., 2008) and displays non-muscle myosin II-dependent pulsed

94    contractions (Franke et al., 2005; Solon et al., 2009), which collectively generate forces that

95    drive migration of the lateral embryonic epidermis. Strikingly, more recent studies have shown

96    that pull forces generated by the amnioserosa layer alone are sufficient to drive DC (Ducuing and

97    Vincent, 2016; Pasakarnis et al., 2016), while supracellular actomyosin cables in the LEs of the

98    lateral embryonic epidermis display ancillary roles in dorsal closure: such as maintenance of

99    epithelial cell packing, tissue organization, and polarity (Ducuing and Vincent, 2016) besides

100   aiding in scar-free zipping (Pasakarnis et al., 2016). In essence, these findings assign

101   degenerating amnioserosa as the major force-generating tissue during DC (for review, see

102   (Hayes and Solon, 2017; Kiehart et al., 2017)).

103   In the light of these emergent understandings of DC, here we have re-examined the roles of a

104   degenerating LEC layer in thorax closure. We show that non-muscle myosin II-mediated

105   contractions along with cell extrusions and cell death in the LEC layer, generate the pull forces

106   that are then relayed to the flanking HEs due to their integrin-based adhesions. Our mathematical

107   modeling further formalizes these biophysical principles underlying LECs-driven tissue closure

108   event, wherein a degenerating, yet dynamic LEC layer drives its succession by the future adult

109   primordia.

110   **Results**

111   *Progressive shrinkage of the LEC layer during thorax closure*

112   In *Drosophila,* thorax closure sets in at an early stage of pupal development—often referred to as

113   'pre-pupal' stage (0-12 hrs after puparium formation (APF) (Fristrom and Fristrom, 1993))—that

4

114    lasts from 4.30 to 6.00 hrs APF at 25□C (Kumar et al., 2020; Martín-Blanco et al., 2000; Usui

115    and Simpson, 2000; Zeitlinger and Bohmann, 1999). Leading-edge (LE) cells of the contralateral

116    HEs—which are seen in close apposition with the underlying LEC layer (Martín-Blanco et al.,

117    2000; Pastor-Pareja et al., 2004; Usui and Simpson, 2000)—display upregulated expression of a

118    JNK reporter, *puc-lacZ* (Figure 1A, A'), besides actin-enriched filopodial and lamellipodial

119    protrusions (red and blue arrows, respectively, Figure 1A').

120    We first re-examined the LEC layer and HE movements and dynamics during thorax closure by

121    live-cell imaging. Nuclei of LECs were selectively marked (*A58>nu-DsRed*, also see Figure

122    S1D) (Anderson and Galko, 2014; Galko and Krasnow, 2004) along with Spider-GFP—reporter

123    for *gish* gene (Morin et al., 2001)—which marks the cell boundaries of both HEs and LECs

124    (Morin et al., 2001) (left panel in Video 1, Figure 1B). We noticed a progressive shrinkage of

125    LEC layer perimeter (left and right panel in Video 1, Figure 1B, and red outlines in Figure 1C)—

126    coincident with the progression of migrating LEs of the contralateral HEs (left panel in Video 1,

127    Figure 1B and green outlines in Figure 1C); with LEC layer displaying a comparable rate of

128    shrinkage (4.1±0.77 µm/min, Figure 1C) to that of HEs migration (4.3±0.46 µm/min for HE,

129    Figure 1C). This shrinkage in the LEC layer results in a precipitous drop in its surface area

130    during thorax closure (4:30 to 6:00 hrs APF, Figure 1D) besides nearly a two-fold increase in its

131    cell density, as seen from nuclear counts in its medial region (Figure 1E, see representative boxes

132    1-3 in Figure 1B).

133    Trajectories of LECs migration—visualized by tracking their nuclear displacements (right panel

134    in Video 1) revealed spatio-temporal characteristics: initial trajectories are aligned along the

135    anterior-to-posterior (A→P) body axis (between 0-4 hrs APF; right panel in Video 1, Figure 1F):

136    that is, when thoracic LECs display apolysis or detachment from the overlaying pupal cuticle

137    (Usui and Simpson, 2000) while later, during thorax closure proper, these trajectories were seen

138    along the L→M axis (4:30-6:00 hrs APF; right panel in Video 1, Figure 1G), parallel to the

139    direction of HEs migration (left panel in Video 1; Figure 1B).

140    Cryo-cross sections along the second thoracic pupal segment (T2) further revealed that LEs of

141    HEs remain in contact with the lateral edges of the LEC layer (Figure 1H-I) (also see (Usui and

142    Simpson, 2000)). Further, we noticed a transition of the LEC layer from flattened squamous

143    cells, with widely-spaced nuclei aligned in a single plane (4:30 hrs APF, red nuclei in Figure 1H)

144    to densely packed tall columnar cells wherein nuclei are seen at different planes along their

145    dorso-ventral axis (5.30 hrs APF, red nuclei in Figure 1I), revealing their transition to a pseudo-

146    stratified state (also see (Norden, 2017)). Moreover, at later stages, LECs were also seen to be

147    extruded from the layer (yellow stars in Figure 1I). Confocal microscopic optical X-Z sections of

148    the LEC layer further confirmed an increase in its cell packaging density (Figure 1K compared to

149    1J), increased cell heights (Figure 1K, L) with accompanying pseudo-stratification (Figure 1K),

150    and, finally, cell extrusion (yellow stars, Figure 1K) during thorax closure.

151    Together, these observations reveal a host of novel features of epithelial dynamics in the LEC

152    layer, which present a compelling argument for a possible link for its active role in thorax

153    closure (Figure 1M).

154    ***Delamination and cell death in the LEC layer facilitate unimpeded HE migration and zipping***

155    Programmed cell death (PCD) is a key event in early embryonic development in both

156    invertebrates and vertebrates (for reviews, see (Nagata, 2018; Singh et al., 2019; Suzanne and

157    Steller, 2013; Teng and Toyama, 2011)). For instance, during DC, PCD in the amnioserosa

158    contributes to generating pull forces that drive tissue closure (Teng and Toyama, 2011; Toyama

159    et al., 2008). Likewise, elimination of abdominal LECs by apoptosis prefigures the expansion of

160    histoblast nests (Ninov et al., 2007; Teng and Toyama, 2011) via a 'push-pull coordination' with

161    the latter (Prat-Rojo et al., 2020). It is therefore conceivable that delamination in LECs (Figure

162    1I, K) and their eventual loss by apoptosis (Ninov et al., 2007) could also be crucial for thorax

163    closure by removing the impediment of cell crowding on the path of migrating HEs.

164    A careful examination of Spider-GFP marked LECs (Figure S2A) revealed their shrinking

165    perimeters (yellow arrows, Figure S2A') while their live imaging using Lachesin-GFP—a

166    septate junction protein reporter (Morin et al., 2001)—further revealed progressive apical

167    constrictions (yellow and red arrows in Video 2 and Figure 2A) and delamination (Figure S2B).

168    Previously, it has been shown that delaminating cells often display apoptosis, marked by caspase

169    activation (Muliyil et al., 2011; Saias et al., 2015; Teng et al., 2017). Indeed, an Apoliner

170    construct—a genetically encoded caspase sensor and an early apoptotic marker (Bardet et al.,

171    2008)—revealed early caspase activation in the majority of LECs (Figure S2C), which reconciles

172    well with the fact that most LECs are delaminated (Figure S2D), leading to their elimination by

173    cell death.

174    To further probe the role of cell death in the LEC layer, we examined the consequences of gain

175    of p35—an inhibitor of caspase-3-like proteins in *Drosophila* (Hay et al., 1994)—by selectively

176    driving *UAS-p35* transgene under the *A58-Gal4* driver (Figure S1D). Comparison of the endpoint

177    of thorax closure, as revealed by X-Y (upper panel, Figure 2B) and X-Z optical sections (lower

178    panel, Figure 2B), at 6:00 hrs APF for the control (*A58>GFP*, Figure 2B) and in case of *p35*

179    overexpression (*A58>GFP; p35*, Figure 2B) revealed cell overcrowding (yellow star, Figure 2B,

180    lower panel) in the latter with an accompanying impediment in HE fusion, as seen from their

181    failed zipping and persistence of large inter-HE gap (arrowheads in Figure 2B, lower panel). Not

182    surprisingly, adults emerging out of these pupae displayed a characteristic cleft-thorax phenotype

183    (arrowhead, Figure 2C) besides the persistence of non-extruded LECs in the freshly eclosed

184    adults (arrowhead, GFP, Figure 2C) and prolongation of the duration of thorax closure (Figure

185    2D). Similar overcrowding and failure in HE fusion can also be seen in the case of *p35*

186    overexpression both in HEs and LECs (Figure S3A) using the *pnr-Gal4* driver (Figure S1B).

187    These adults also displayed the characteristic cleft-thorax phenotype (arrowhead in the upper

188    panel of Figure S3B) and persistence of non-extruded LECs in freshly eclosed adults (arrowhead

189    in the lower panel of Figure S3B), besides prolonging the duration of thorax closure (Figure

190    S3C). By contrast, a selective overexpression of *p35* in only the HEs, using *332.3Gal80; pnr-*

191    *Gal4* (see Figure S2D) did not affect thorax closure (Figure S3D).

192    Together, these results reveal that cell death in the LEC layer aid in its shrinkage, help reduce

193    overcrowding of LECs and, facilitate HE migration and fusion during thorax closure (Figure 2E).

194    ***Non-muscle myosin-II-mediated contraction in LEC layer drives migration of HEs***

195    Given the possible active contraction (Video 2, Figure 2A) and overall shrinkage in the LEC

196    layer (Video 1, Figure 1), it is likely that during thorax closure it can generate pull forces that

197    facilitate HE migration. To test this possibility, we first ablated the LEC layer using a short pulse

198    of the laser during thorax closure and visualized the fallouts (red arrow in Video 3). Indeed,

199    ablation of the LEC layer during thorax closure brings HE migration to a halt, which then

200    recedes away (red stars in Figure 3B compared to 3A, Video 3 compared to left panel in Video

201    4) as seen from a rapid increase in their inter-HE distance (red stars, Figure 3B and C). This

202    fallout of the laser ablation in the LEC layer, therefore, suggests that the LEC layer is under

203    tension and can generate pull forces. Conversely, it may also be argued that laser ablation

204    disrupts the LEC layer, thereby disrupting the scaffold over which contralateral HE migrates

205    (Martín-Blanco and Knust, 2001; Martín-Blanco et al., 2000).

206    To distinguish between the two alternative roles of the degenerating thoracic LEC layer during

207    thorax closure: namely, its role as a passive scaffold versus active contractile force generator, we

208    further asked if, like the contractile amnioserosa cells (Franke et al., 2005; Young et al., 1993),

209    LECs, too, display non-muscle myosin II-dependent contractions. We examined the expression

210    of the regulatory light chain of non-muscle myosin II, *spaghetti squash (sqh)*—based on its GFP

211    reporter, Sqh-GFP (Sisson et al., 2000)—during the thorax closure. Sqh regulates non-muscle

212    myosin II contractile functions via its phosphorylation (Vereshchagina et al., 2004). We noticed

213    an elevated Sqh-GFP level in LECs (Figure 3D-D'') and also in the LEs of the contralateral HE

214    (Figure 3D), reminiscent of the domains of expression of Zip/Myo-II in analogous cell types in

215    the embryonic dorsal closure: that is, amnioserosa and the LE of the lateral epidermal layer,

216    respectively (Franke et al., 2005). LECs also displayed enrichment of actin, which co-localized

217    with Sqh-GFP on the cell edges and also in their cytoplasm (Figure 3D-D''') (Franke et al., 2005;

218    Gorfinkiel, 2016).

219    To assess the functional relevance of Sqh enrichment in the LEC layer during thorax closure, we

220    knocked down *sqh* simultaneously in both the LEC layer and the HE (Figure S1B) (left panel in

221    Video 5 compared to left panel in Video 4), selectively in only the LEC layer (Figure S1D)

222    (middle panels in Video 5 compared to the middle panel in Video 4) or in the HE (Figure S2C)

223    (right panel in Video 5 compared to the right panel in Video 4). We noticed a failure in thorax

224    closure when the *sqh*-knockdown spanned the LEC layer (double arrow in left and middle panel

225    in Video 5, Figure 3E and 3F). Quantification of the inter-HE distances at various time intervals

226    of thorax closure following *sqh* knockdown in the LECs or both in LECs and HEs, further

227    revealed persistent gaps and failed closure (red and blue bars in Figure 3H). We also note that

228    knockdown of *sqh* in HEs does not have much impact on thorax closure (right panel in Video 5,

229    Figure 3G and green bars in Figure 3H), reminiscent of the possible redundant role of LEs in DC

230    ((Franke et al., 2005) for review see (Kiehart et al., 2017)).

231   Thus, during thorax closure, as in DC, pull forces generated by non-muscle myosin II from the

232   LECs drive the HE migration, which is reminiscent of the role played by amnioserosa during

233   dorsal closure (for review, see (Kiehart et al., 2017)).

234   ***Pull forces from the LEC layer are relayed to the contralateral HE via their integrin-based***

235   ***adhesion***

236   Adhesion between two apposed cell layers can impact their respective morphogenesis and

237   mechano-transduction (Sun et al., 2016). Such inter-tissue adhesions are often mediated by the

238   members of the integrin family, comprising of α and β subunits of position-specific (PS)

239   integrins (Narasimha and Brown, 2013). For instance, during embryonic DC, the lateral

240   embryonic epidermal layers adhere to the centrally placed amnioserosa via enrichment of βPS1

241   (Myospheroid, Mys) and αPS3 (Scab, Scb) dimers at their tissue interfaces, thereby facilitating

242   relay of forces between these two cell layers (Narasimha and Brown, 2004).

243   We thus examined the fallouts of knockdowns of integrins during thorax closure. *Drosophila*

244   genome encodes 2β (βPS1 and βν) and 5α (αPS1-5) subunits of integrins that form multiple

245   versions of heterodimeric (αβ) integrin complexes in different contexts of embryonic and adult

246   development (Narasimha and Brown, 2004; Narasimha and Brown, 2013). Individual

247   knockdowns using RNAi constructs of 2β and 4α (αPS1-4) integrins in both HE and LECs

248   (Figure S1B) showed very high pupal lethality upon *mys ($\beta$-PS1)* or *scb ($\alpha$-PS3)* knockdown,

249   suggesting their possible involvement in thorax closure (Figure S4A) while rest eclosed as adults

250   without thorax closure defect (Figure S4A).

251   A Mys-GFP reporter further revealed Mys enrichment at the HE-LEC layer contact points

252   (Figure 4A-B) besides their enrichment at apico-lateral cell edges in both tissues (Figure 4B', B''

253   and their Y-Z optical sections). Further, knockdown of *mys* in both HE and LEC layer (see

254   Figure S1B) or only the LEC layer (see Figure S1C) disrupted the process of thorax closure

255   (double-headed arrow in left and middle panel in Video 6), culminating from the loss of LEC-HE

256   contacts, besides the loss of LEC layer integrity, as seen from the loss of cell-cell contacts

257   (yellow arrows in left and middle panel in Video 6, Figure 4C, D). By contrast, selective

258   knockdown of *mys* only in the HE was marked by a characteristic snapping of the HE during the

259   migration process from the LEC layer and culminating in a failed zipping of HEs (red arrow in

260    the right panel of Video 6) besides detachment of the two cell layers (Figure 4E). These extreme

261    phenotypic consequences of *mys* loss precluded adult emergence (Figure S4A). We thus

262    compromised Gal4 expression by raising the larval cultures at a lower growth temperature

263    (18$^o$C) (see Material and Methods) (Duffy, 2002), which results in the eclosion of adults from

264    ~30% of these pupae, which invariably displayed cleft-thorax phenotype (Figure 4F-I).

265    Additionally, live imaging from knockdown of *scb* in both LECs and HEs (Figure S4B) or LECs

266    alone (Figure S4C), too, revealed an arrest of HE migration and loss of LEC layer integrity—like

267    those seen following *mys* knockdown (Figure 4C-D). It is, therefore, likely that βPS1 (Mys) and

268    αPS3 (Scb)—presumably as heterodimeric partners (Narasimha and Brown, 2004; Narasimha

269    and Brown, 2013)—maintain LEC-HE adhesion—which is essential for the relay of pull forces

270    from the LEC layer to HE.

271    ***Epithelial dynamics in the LEC underlies thorax closure – an in-silico analysis***

272    To test the biophysical underpinnings of this emergent mechanism of thorax closure, we utilized

273    a two-dimensional vertex model of the LEC layer along with two flanking contralateral HEs. The

274    vertex models have been utilized extensively to study epithelial mechanics in several

275    developmental contexts, such as oriented cell divisions (Mao et al., 2011), density-independent

276    phase transitions (Bi et al., 2015), epithelial topology (Aegerter-Wilmsen et al., 2010), cell flows

277    during epithelial morphogenesis (Aigouy et al., 2010), cell size oscillations (Lin et al., 2017) or

278    cell-cell adhesion mediated cell size dynamics (Kumar et al., 2020). In our vertex model, the

279    mechanical response of the cells (LECs as well as HEs) is characterized by an energy function

280    (Figure 5A) comprising of contributions from cell elasticity arising due to impermeability, or

281    absence of leakiness of cell membrane, actomyosin-driven cell contractility and cadherin or

282    integrin (at the interface of LEC layer and HE) mediated cell-cell adhesion (Farhadifar et al.,

283    2007; Kumar et al., 2020). For overdamped cellular dynamics, the velocities of vertices are taken

284    as proportional to the forces which are calculated from derivative of the energy functional

285    relative to the vertex positions (Figure 5A, see Materials and methods).

286    The numerical simulation of the vertex model of LEC and HE recapitulates the experimental

287    observations, as shown (first panel in Video 7, Figure 5B). Starting from irregular cell geometries

288    in the LEC layer, cells are seen to elongate along the L→M direction due to higher drag offered

289    by the HE (Figure 5B), reminiscent of such transitions seen *in vivo*. Further, in the absence of

290    active forces, mediated by Sqh and delamination, in the LECs *in vivo* resulted in arrested thorax

291    closure (second and third panel in Video 7, Figure 5C and 5D). Finally, lowering of cell contacts

292    between LECs and HEs—representing the fallout of *in vivo* knockdown of integrins in HE-

293    specific manner (see Figure S1C) (fourth panel in Video 7)—arrested HE migration and thorax

294    closure (Figure 5E). These findings from vertex simulation, therefore, further reaffirm that LEC

295    delamination and contraction-mediated pull forces relayed to HE are essential biophysical

296    principles of thorax closure.

## Discussion

298    A comparison between embryonic DC and pupal thorax closure reveals uncanny parallels

299    between their respective LEs: both leading their respective epithelia all the way to migrate over a

300    degenerating cell layer of a preceding developmental stage (Belacortu and Paricio, 2011;

301    Zeitlinger and Bohmann, 1999). Given the primary importance assigned earlier to the LEs for the

302    migration of embryonic lateral epidermis during DC (Kiehart et al., 2000), it may appear

303    reasonable to assume LEs as a force-generator during thorax closure (Martín-Blanco et al.,

304    2000). Instead, our results reveal that it is the LEC layer generated pull forces that are necessary

305    during the thorax closure. During thorax closure, the LEC layer displays elaborate orchestration

306    of epithelial dynamics marked by squamous-to-pseudostratified columnar transition and

307    accompanying the non-muscle myosin-II-mediated contractions, cell extrusion and cell death.

308    Pull forces, thus generated in the shrinking LEC layer, are then relayed to the flanking HEs via

309    their mutual integrin-based adhesions (Figure 6). From the biomechanical viewpoint, too, our

310    simplified two-dimensional vertex model formalizes these essential elements of the LEC layer in

311    thorax closure: namely, their cell delamination, non-muscle myosin-II driven contractions and

312    finally its integrin-based adhesion with HEs (Figure 5). In essence, therefore, reminiscent of

313    embryonic amnioserosa ((Ducuing and Vincent, 2016; Pasakarnis et al., 2016) for review see,

314    (Hayes and Solon, 2017; Kiehart et al., 2017)), the degenerating thoracic LEC layer, too,

315    generates the forces required to drive its replacement by successors—the HEs.

316    *LEC generates the pull forces for HE migration*

317      Our results reveal two core attributes of the LEC layer, which underlie HE migration. The first

318      attribute is its non-muscle myosin II-mediated contractions. It is conceivable that actomyosin-

319      mediated contraction of the LECs, too, contribute to their cell shape remodeling, reminiscent of

320      other morphogenetic processes, such as gastrulation, oogenesis, and intercalation during

321      germband elongation (for review, see (Heisenberg and Bellaïche, 2013)). For instance, deep

322      tissue imaging of *Drosophila* gastrulation reveals that apical actomyosin meshwork drives apical

323      contraction in the ventral furrow cells leading to cell lengthening and basal movement of the

324      nuclei: the net fallout being volume conservation within a constrained space (Gelbart et al., 2012;

325      Khan et al., 2014). During thorax closure, too, the LECs display apical contractions (see Video 2,

326      Figure 2A) and cell elongation (Figure 1I and K-L)—accompanying their squamous-to-columnar

327      epithelial transition—which could also mean their volume conservation during cell shape

328      remodeling (for review (Gorfinkiel, 2016)). Further, the apical enrichment of actin and Sqh

329      (Figure 3D-D''') in the LEC layer during thorax closure not only generates pull forces but could

330      as well be responsible for an increase in cell density. A consequent cell overcrowding in the LEC

331      layer on the other hand is offset by cell extrusion and cell death (Figure 6). This essential

332      attribute of the LECs are also seen in amnioserosa during DC, marked by cell extrusions

333      (ingression) via apoptosis ((Toyama et al., 2008) for review, see (Ambrosini et al., 2017; Kiehart

334      et al., 2017; Teng and Toyama, 2011)). In other migrating epithelia, too, such as the HEs, cell

335      overcrowding-mediated cell extrusion alleviate space constraint, leading to restoration of cell

336      number homeostasis ((Levayer et al., 2016; Marinari et al., 2012) for review, see (Ambrosini et

337      al., 2017; Fadul and Rosenblatt, 2018)).

338      The second core attribute of the LEC layer is its integrin-based adhesion with the flanking HEs

339      that allow relay of the pull forces to the latter (Figure 6). This scenario, too, appears to recur in

340      multiple contexts of animal development, including DC in *Drosophila* embryogenesis (Muliyil et

341      al., 2011; Narasimha and Brown, 2004) or in mouse embryos wherein surface ectoderm

342      connecting contralateral neuroepithelium—the precursor to the neural tube—display enriched

343      levels of integrin β1 subunit apically (Molè et al., 2020).

344      ***Thorax closure: an archetypal mechanism for tissue or wound closure***

345　One of the enduring revelations of various tissue closure mechanisms during development or

346　tissue repair is the critical role of the cell death in the degenerating cell layer. For instance,

347　during wound healing, injured and dying cells send out a signal—both humoral (cytokine) and

348　mechano-stimuli—to the surrounding healthy cells to migrate and proliferate and thereby leading

349　to their replacement (for review, see (Eming et al., 2007; Gurtner et al., 2008; Martin, 1997;

350　Shaw and Martin, 2009)). For instance, a wounded site is marked by aggregation of

351　myofibroblasts, which represent transformed fibroblasts (Alberts et al., 2002) or are derived from

352　epithelial cells through EMT (Yang and Liu, 2001). These are enriched in stress fibers and thus

353　generate contractile forces to bring the wound edges closer. Upon wound healing, myofibroblasts

354　are eliminated by apoptosis (Darby et al., 2014; Li and Wang, 2011). LECs, too, display

355　functional parallels with myofibroblasts at wound sites. For instance, while these LECs remain

356　dormant during larval life, their secretory activities are heightened upon pupariation and secretes

357　of pre-pupal cuticle (Fristrom and Fristrom, 1993). Further, reminiscent of fibroblasts-to-

358　myofibroblasts transition upon tissue injury, abdominal LECs, too, display EMT-like transition

359　marked by filopodial and lamellipodial protrusions (Arata et al., 2017; Bischoff, 2012). These

360　uncanny parallels between LECs *in situ* during thorax closure and the myofibroblasts, which

361　migrate at the site of tissue closure, further show that the principles of thorax closure revealed

362　here are primitive, presumably predating the emergence of holometabolous insects, and have

363　been co-opted for multiple contexts of developmentally regulated tissue closure and repair

364　events.

365　**Materials and Methods**

366　 *Fly stocks and rearing conditions*

367　Stocks used in this study include:

368　**Gal4 lines:** *pnr-Gal4* (Chr. III) (Calleja et al., 2000) and *A58-Gal4* (Chr. III) (Galko and

369　Krasnow, 2004).

370　**Gal80 lines:** *332.3Gal80* (Chr. II) (Pasakarnis et al., 2016).

371　**UAS-based reporter lines:** *UAS-(nls)GFP* (Chr. III) (BDSC #4776), *UAS-nuDsRed* (Chr. III)

372　(Galko and Krasnow, 2004), and *UAS-Apoliner* (Chr. II) (BDSC #321122) (Bardet et al., 2008).

373    **UAS-overexpression lines:** *UAS-p35* (Chr. X) (BDSC #6298).

374    **UAS-knockdown lines:** *UAS-sqh-RNAi* (Chr. III) (BDSC #33892), *UAS-Itgbn-RNAi (βυ)* (Chr.

375    III) (BDSC #28601), *UAS-mys-RNAi (βPS)* (Chr. III) (BDSC #27735), *UAS-mew-RNAi*

376    *(☐PS1)*(Chr. III) (BDSC #27543), *UAS-if-RNAi (☐PS2)* (Chr. III) (BDSC #27544), *UAS-scb-*

377    *RNAi (αPS3)* (Chr. III) (BDSC #27545), and *UAS-ItgaPS4-RNAi (αPS4)* (Chr. III) (BDSC

378    #28535).

379    **Reporter lines:** *puc-LacZ$^{E69}$* (Chr. III) (Martín-Blanco et al., 1998), *mys-GFP* (Chr. X)

380    (Klapholz et al., 2015), *sqh-GFP* (Chr. II) (BDSC # 57145), *lac-GFP* (BDSC #6833) (Morin et

381    al., 2001) and *spider-GFP* (Chr. III) (BDSC #59025) (Morin et al., 2001).

382    All fly cultures, unless mentioned otherwise, were grown at 25±1°C on standard fly food.

383    Knockdown or overexpression-based studies were performed on 25±1°C. For *mys* adult studies,

384    second-instar larvae were transferred to 18°C to decrease Gal4 activity (Duffy, 2002) and rescue

385    high pupal lethality.

### *Staging, dissection, and immunostaining of pupal HE*

387    0 hrs APF pupae were carefully selected and dissected at desired time points, as described

388    previously (Kumar et al., 2020). In brief, dissection was performed and fixed in 4% PF in 1X

389    PBST followed by 1X PBST washes and antibody staining. Primary antibody and their dilutions

390    used were: anti-Lgl (1:50) (Gift from Fumio Matsazaki) and β-galactosidase (1:200) (raised in

391    mouse; Sigma Aldrich, Catalog No: G8021). Secondary antibodies used were tagged with Alexa

392    488, 555, or 633 (Molecular Probes). Phalloidin (488, 555 or 633) and ToPro (555 or 633) were

393    used to mark F-actin filaments and nucleus, respectively. Final mounting was done in

394    Vectashield (H-1000, Molecular Probe) using a bridge slide.

### *Pupal cryo-cross section preparations*

396    For the pupal cryosections, staged samples were fixed overnight with 4% PF in 1X PBS at 4$^{o}$C

397    followed by washing in 0.1% PBST and treatment with graded sucrose (10, 20, and finally in

398    30%). Later, the samples were treated in an OCT (Leica Biosystems, Product No. 3801480) and

399    30% sucrose media (1:1) before final mounting in the OCT followed by freezing. 15 μm thick

400    sections were cut using Leica cryotome, counterstained, and mounted in lysine coated glass

401    slides.

### *Image acquisition and processing*

403    For whole-mount and cryosection preparations, confocal images were acquired using the Leica

404    SP5 laser scanning confocal microscope. Pupal (still and time-lapse) and adult imaging were

405    performed using Leica M205FA or Zeiss AxioZoom V1.6 microscope on either bright field or

406    GFP filters. Images were processed using LAS 4.0, ImageJ software, and Adobe Photoshop CS6,

407    whichever relevant.

### *Laser ablation in LEC layer*

409    A modified FRAP protocol was used in a tunable infrared laser attached to Leica multiphoton

410    SP8 confocal microscope to ablate the LEC layer. Initially, the staged pupae (4:30 hrs APF) was

411    imaged for 30 mins (30 seconds per frame) to reach 5 hrs APF and shifted to FRAP conditions

412    where 100% laser at 900 nm was focused in a narrow rectangular ROI (red box, Figure 3B) on

413    the LEC layer for 60 secs and imaged again in normal conditions for 15 mins (30 sec per frame)

414    (Video 3).

### *Calculation of inter-HE distance*

416    Inter-HE distances during various perturbations was calculated based on measuring the L→L

417    distance between migrating leading edges of the HE. The graph was then plotted in GraphPad

418    8.0.

### *Quantification of various LEC layer parameters*

### *LEC surface area:*

421    For the measurement of the LEC layer surface area over time, outlines were manually drawn

422    along the perimeter of the LEC layer with Nu-DsRed marked nucleus (*A58>nu-DsRed*) on

423    selected time-lapse images during thorax closure. The surface areas were then measured using

424    ImageJ software.

425   *LEC nucleus number:*

426   For counting the nuclear number in the LEC layer, live imaging video of Nu-DsRed marked

427   nuclei (*A58>Nu-dsRed*) (right panel in Video 1) was used, and nuclei numbers were counted

428   using the particle analyzer tool in ImageJ.

429   *LEC layer crowding:*

430   Three boxes of equal size were placed in the medial LEC layer (Box 1 and 2 on T2 and Box 3 in

431   T3 segments), followed by manual counting and plotting in Excel.

432   *LEC nuclear migration:*

433   Each frame of the right panel in Video 1 with *A58>Nu-dsRed* stained nuclei was smoothened

434   using a Gaussian filter followed by image thresholding. The location of each nucleus in each

435   frame was subsequently detected by finding the local maxima in the image with skimage Python

436   library. For movie frames corresponding to 0-4 hrs APF and 4-6 hrs APF, the location of the

437   nucleus was plotted using scatter plots, in blue and green colors, respectively.

438   *LEC layer thickness:*

439   Y-Z sections were used to calculate the thickness of the LEC layer (*pnr>GFP)* of pupae at two

440   different time points, before and during thorax closure. Image analysis was performed on LAS-X

441   software followed by their plotting on GraphPad Prism 8.0.

442   *Mathematical model:*

443   *Introduction to vertex model of epithelium*

444   Vertex modeling is a handy tool for the study of the biophysical mechanisms in the epithelial

445   tissues, which is a three-dimensional structure, by the representation of apical cross-sections of

446   the cells with an assumption that the cell geometry does not change as one moves from the apical

447   to the basal end of a cell. Vertex modeling permits the testing of the essential elements of the

448   LEC dynamics and its relay to the HE in a highly simplified version posed side by side (Bi et al.,

449   2015; Farhadifar et al., 2007; Kumar et al., 2020). Further, the epithelial dynamics has been

16

450    considered in the vertex model to be intrinsically regulated based on the features embedded in

451    itself, and thus do not factor the precise trajectories of LEC shrinkage displayed by LEC apolysis

452    and during the thorax closure proper (see Figure 1). Further, confluent LEC and heminota in a

453    monolayer in our vertex model is not an exact representation of these tissue alignments seen *in*

454    *vivo,* where these are seen in different planes. Furthermore, the two-dimensional vertex-based

455    representation also does not consider the contributions other than that of LEC and HE cells, such

456    as thorax geometry, the effect of the larval segment boundaries, or even the activity of the

457    muscular layer underlying the LEC layer. These simplifications notwithstanding, vertex

458    modeling allows substantial resolution of the biophysical underpinning of the LEC dynamic and

459    its fallout on the HEs.

460    In this reduced two-dimensional framework, the mechanics of an epithelial monolayer is

461    described by the energy functional:

$$E(\mathbf{R}_i) = \sum_{\alpha} \frac{K_\alpha}{2}(A - A_\alpha)^2 + \sum_{\alpha} \frac{\Gamma_\alpha}{2} L_\alpha^2 + \sum_{\alpha,\beta} \Lambda_{\alpha,\beta}\, l_{\alpha,\beta} \qquad (1)$$

$$\mathbf{f}_\alpha(\alpha, \mathbf{R}_i) = g\big(M(\alpha)\big)\mathbf{n}(\mathbf{R}_i) \qquad (2)$$

462    where $K_\alpha$ represents the modulus of area elasticity for cell- $\alpha$, which is, in this context, a

463    combined manifestation of the incompressibility of cytoplasm and impermeability of the cell

464    membrane, $\Lambda_{\alpha,\beta}$ incorporates the cadherin dependent cell-cell adhesion at the edge shared

465    between two adjacent cells $\alpha$ and $\beta$, and, finally, $\Gamma_\alpha$ stands for cell contractility arising due to the

466    actomyosin network near the apical end of the cell. Following the approach proposed earlier, we

467    can non-dimensionalize the adhesion parameter and contractility by $K_\alpha A_o^{3/2}$ and $K_\alpha A_o$,

468    respectively (Farhadifar et al., 2007).

469    From the energy functional, one can calculate the force acting on each vertex by taking the

470    functional derivative of the above equation for the vertex coordinates. Under the assumption of

471    overdamped dynamics, the velocity of each vertex is proportional to the total force acting on it.

472    *T1 transition:* In addition to the vertex movements due to the forces acting on it, in this model T1

473    transition is also taken into account where a collective of four cells exchange some of their

17

474    neighbors (see Figure M1A). The T1 transition occurs whenever the edge, shared between any

475    two cells, becomes smaller than a pre-specified threshold value.

476    *T2 transition:* Further, whenever the two-dimensional apical cross-section of a cell becomes

477    smaller than a pre-specified threshold value, the cell is considered to get detached from the

478    epithelial monolayer (see Figure M1A). It can be understood by the fact that a minimal cell in the

479    vertex model, which is a two-dimensional representation of apical end only, implies that most of

480    its contents are already out of the plane of the tissue, and the cell is destined to get delaminated

481    from the tissue. This process is known as the T2 transition.

482    With this description of the basic vertex model (without any tissue-specific ingredients) in the

483    following, we will describe the tissue-specific model considerations.
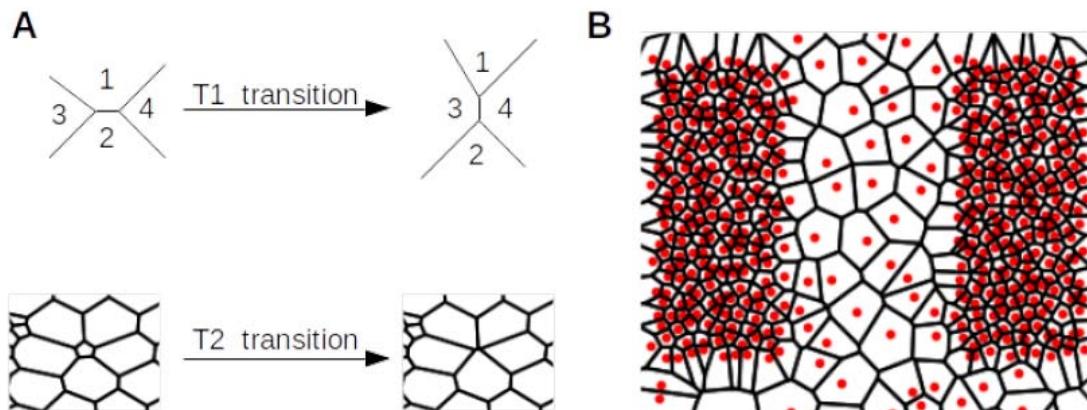


484    **Figure M1: (A)** Schematic depicting T1 and T2 transitions. **(B)** The generation of initial cell

485    configurations for the LEC layer and HE. The red dots denote the initial seeds for the Voronoi

486    tessellation with sparse and dense red dots representing LEC and HE, respectively.

487    *Initial cell geometry generation*

488    For the study of the LEC dynamics, we utilize the same framework while considering both of the

489    LEC and two flanking contralateral HEs. It is worth recalling here that even though both the

490    tissues are epithelial, their detailed descriptions differ significantly since LECs are of squamous

491    characteristics (large apical section), and HE cells are of columnar type (smaller apical section).

492    To generate a monolayer of LEC with HE for the vertex model, we use Voronoi tessellation with

493    the seed points with higher and lower densities in the HE and LEC regions, respectively (see

494    Figure M1B).

*Vertex model for HE*

496    For the modeling of the HE cells, we utilize the vertex model without any additional

497    consideration. Although, as reported in one of our earlier works, the dynamics of the HE cells is

498    regulated by the expression gradients of members of the planar cell polarity pathway, we do not

499    take that detail into account here (Kumar et al., 2020). We do not expect the findings to change

500    even if those details are incorporated into the model.

*Vertex model for LEC layer*

502    For the LEC layer, we extend the vertex model to incorporate the role of the Sqh, as observed in

503    the experiments. We take into account the contractile activity of the Sqh in the form of active

504    forces on the boundaries of the LEC cells in the direction normal to the cell membrane. The

505    active force on the $i^{th}$ vertex of the cell is:

$$\mathbf{f}_\alpha(i) = \mathcal{H}(\boldsymbol{M}_s(i))\boldsymbol{n}_i \tag{3}$$

506    where, $\mathcal{H}$ is the Hill's function, $\boldsymbol{M}_s$ is the level of Sqh in the cell and $\boldsymbol{n}_i$ is the membrane inward

507    normal at the $i^{th}$ vertex. This nature of active forces has previously been used to model motile

508    cells of amoeboid nature (Farutin et al., 2013). It has to be noted that due to the intrinsic nature

509    of the active force, the total active forces and total torque due to the active force on the cell

510    should vanish. That is:

$$\oint \mathbf{f}_\alpha \, dl = 0, \oint \mathbf{r} \times \mathbf{f}_\alpha dl = 0 \tag{4}$$

511    where, the integrals are along the cell perimeter. In order to ensure this, we add a correction to

512    the active forces in the form:

$$\mathbf{f}_c(i) = \mathbf{f}_0 + f_t \mathbf{t}_i \tag{5}$$

19

513     where $\mathbf{t}_i$ is the unit vector tangent to the cell membrane. The exact values of the $\mathbf{f}_0$ and $f_t$ are

514     calculated from equation (4). These corrections ensure that the total active force and torque on

515     each cell vanish (Wu et al., 2016). For the LECs, we considered that the level of Sqh is equal in

516     all the cells. To keep the computer simulation of the model, we apply active forces in a ramping

517     manner starting from 0 to a fixed maximum value in linear increment over time.

518     **Boundary conditions**

519     Forces from the boundaries play a significant role in the overall dynamics of the epithelial tissues

520     (Cochet-Escartin et al., 2014; Nikolić et al., 2006) and are so expected in thorax closure. In the

521     simulation of thorax closure, we have considered all the boundaries to be stress-free. It needs to

522     be pointed out that this boundary condition represents a simplification of the *in vivo* condition

523     where the tissues and geometric features, such as the segment boundary, adjacent to the LEC or

524     HE may present additional constraints to the cell dynamics.

525     **Simulation of different cases shown in Figure 5**

526     Figure 5 shows the results of vertex modeling of the thorax closure with the following cases:

527     **1.** The Wild-type case (Figure 5B) considers all the aforementioned model ingredients.

528     **2.** For the simulation of LEC layer dynamics with no Sqh (Figure 5C), we reduced the value of

529     Sqh to $1/10^{\text{th}}$ of the Wild type case.

530     **3.** For the simulation with no cell delamination (Figure 5D), the T2 transitions were not

531     performed.

532     **4.** For the simulation with integrin loss (Figure 5E) the adhesion between the LECs and the HE

533     cells was broken.

540    for their help in tissue cryo-sectioning.

541

545

546    **References**

547    **Aegerter-Wilmsen, T., Smith, A. C., Christen, A. J., Aegerter, C. M., Hafen, E. and Basler,**
548         **K.** (2010). Exploring the effects of mechanical feedback on epithelial topology.
549         *Development* **137**, 499–506.

550    **Agnès, F., Suzanne, M. and Noselli, S.** (1999). The *Drosophila* JNK pathway controls the
551         morphogenesis of imaginal discs during metamorphosis. *Development.* **126**, 5453–5462.

552    **Alberts, B., Johnson, A., Lewis, J., Raff, M., Roberts, K. and Walter, P.** (2002). Fibroblasts
553         and Their Transformations: The Connective-Tissue Cell Family. *Molecular Biology of*
554         *the Cell, 4th Ed.* Garland Science.

555    **Ambrosini, A., Gracia, M., Proag, A., Rayer, M., Monier, B. and Suzanne, M.** (2017).
556         Apoptotic forces in tissue morphogenesis. *Mech. Dev.* **144**, 33–42.

557    **Anderson, A. E. and Galko, M. J.** (2014). Rapid clearance of epigenetic protein reporters from
558         wound edge cells in *Drosophila* larvae does not depend on the JNK or PDGFR/VEGFR
559         signaling pathways. *Regeneration* **1**, 11–25.

560    **Arata, M., Sugimura, K. and Uemura, T.** (2017). Difference in Dachsous Levels between
561         Migrating Cells Coordinates the Direction of Collective Cell Migration. *Dev. Cell* **42**,
562         479-497.e10.

563    **Aigouy, B., Farhadifar, R., Staple, D. B., Sagner, A., Röper, J. C., Jülicher, F., & Eaton, S..**
564         (2010). Cell flow reorients the axis of planar polarity in the wing epithelium of
565         *Drosophila. Cell* **142**,.

566    **Bardet, P.-L., Kolahgar, G., Mynett, A., Miguel-Aliaga, I., Briscoe, J., Meier, P. and**
567         **Vincent, J.-P.** (2008). A fluorescent reporter of caspase activity for live imaging. *Proc.*
568         *Natl. Acad. Sci. U. S. A.* **105**, 13901–13905.

569    **Beira, J. V. and Paro, R.** (2016). The legacy of *Drosophila* imaginal discs. *Chromosoma* **125**,
570         573–592.

571    **Belacortu, Y. and Paricio, N.** (2011). *Drosophila* as a model of wound healing and tissue
572         regeneration in vertebrates. *Dev. Dyn.* **240**, 2379–2404.

573 **Bi, D., Lopez, J. H., Schwarz, J. M. and Manning, M. L.** (2015). A density-independent
574         rigidity transition in biological tissues. *Nat. Phys.* **11**, 1074–1079.

575 **Bischoff, M.** (2012). Lamellipodia-based migrations of larval epithelial cells are required for
576         normal closure of the adult epidermis of *Drosophila*. *Dev. Biol.* **363**, 179–190.

577 **Cochet-Escartin, O., Ranft, J., Silberzan, P. and Marcq, P.** (2014). Border Forces and
578         Friction Control Epithelial Closure Dynamics. *Biophys. J.* **106**, 65–73.

579 **Darby, I. A., Laverdet, B., Bonté, F. and Desmoulière, A.** (2014). Fibroblasts and
580         myofibroblasts in wound healing. *Clin. Cosmet. Investig. Dermatol.* **7**, 301–311.

581 **Ducuing, A. and Vincent, S.** (2016). The actin cable is dispensable in directing dorsal closure
582         dynamics but neutralizes mechanical stress to prevent scarring in the *Drosophila* embryo.
583         *Nat. Cell Biol.* **18**, 1149–1160.

584 **Duffy, J. B.** (2002). GAL4 system in *Drosophila*: A fly geneticist's swiss army knife. *genesis*
585         **34**, 1–15.

586 **Eming, S. A., Krieg, T. and Davidson, J. M.** (2007). Inflammation in Wound Repair:
587         Molecular and Cellular Mechanisms. *J. Invest. Dermatol.* **127**, 514–525.

588 **Fadul, J. and Rosenblatt, J.** (2018). The forces and fates of extruding cells. *Curr. Opin. Cell*
589         *Biol.* **54**, 66–71.

590 **Farhadifar, R., Röper, J.-C., Aigouy, B., Eaton, S. and Jülicher, F.** (2007). The influence of
591         cell mechanics, cell-cell interactions, and proliferation on epithelial packing. *Curr. Biol.*
592         *CB* **17**, 2095–2104.

593 **Farutin, A., Rafaï, S., Dysthe, D. K., Duperray, A., Peyla, P. and Misbah, C.** (2013).
594         Amoeboid Swimming: A Generic Self-Propulsion of Cells in Fluids by Means of
595         Membrane Deformations. *Phys. Rev. Lett.* **111**, 228102.

596 **Franke, J. D., Montague, R. A. and Kiehart, D. P.** (2005). Non muscle myosin II generates
597         forces that transmit tension and drive contraction in multiple tissues during dorsal
598         closure. *Curr. Biol. CB* **15**, 2208–2221.

599 **Fristrom, D. K. and Fristrom, J. W.** (1993). The metamorphic development of the adult
600         epidermis. *The development of Drosophila melanogaster* **2**, 843-849

601 **Galko, M. J. and Krasnow, M. A.** (2004). Cellular and Genetic Analysis of Wound Healing in
602         *Drosophila* Larvae. *PLOS Biol.* **2**, e239.

603 **Gelbart, M. A., He, B., Martin, A. C., Thiberge, S. Y., Wieschaus, E. F. and Kaschube, M.**
604         (2012). Volume conservation principle involved in cell lengthening and nucleus
605         movement during tissue morphogenesis. *Proc. Natl. Acad. Sci. U. S. A.* **109**, 19298–
606         19303.

607 **Gorfinkiel, N.** (2016). From actomyosin oscillations to tissue-level deformations. *Dev. Dyn.*
608       **245**, 268–275.

609 **Gurtner, G. C., Werner, S., Barrandon, Y. and Longaker, M. T.** (2008). Wound repair and
610       regeneration. *Nature* **453**, 314–321.

611 **Gustafson, T.** (1963). Cellular mechanisms in the morphogenesis of the sea urchin embryo. Cell
612       contacts within the ectoderm and between mesenchyme and ectoderm cells. *Exp. Cell*
613       *Res.* **32**, 570–589.

614 **Harden, N.** (2002). Signaling pathways directing the movement and fusion of epithelial sheets:
615       lessons from dorsal closure in *Drosophila*. *Differentiation* **70**, 181–203.

616 **Hay, B. A., Wolff, T. and Rubin, G. M.** (1994). Expression of baculovirus P35 prevents cell
617       death in *Drosophila*. *Development* **120**, 2121–2129.

618 **Hayes, P. and Solon, J.** (2017). *Drosophila* dorsal closure: An orchestra of forces to zip shut the
619       embryo. *Mech. Dev.* **144**, 2–10.

620 **Heisenberg, C.-P. and Bellaïche, Y.** (2013). Forces in Tissue Morphogenesis and Patterning.
621       *Cell* **153**, 948–962.

622 **Jacinto, A., Woolner, S. and Martin, P.** (2002). Dynamic Analysis of Dorsal Closure in
623       *Drosophila*: From Genetics to Cell Biology. *Dev. Cell* **3**, 9–19.

624 **Khan, Z., Wang, Y.-C., Wieschaus, E. F. and Kaschube, M.** (2014). Quantitative 4D analyses
625       of epithelial folding during *Drosophila* gastrulation. *Development* **141**, 2895–2900.

626 **Kiehart, D. P., Galbraith, C. G., Edwards, K. A., Rickoll, W. L. and Montague, R. A.**
627       (2000). Multiple forces contribute to cell sheet morphogenesis for dorsal closure in
628       *Drosophila*. *J. Cell Biol.* **149**, 471–490.

629 **Kiehart, D. P., Crawford, J. M., Aristotelous, A., Venakides, S. and Edwards, G. S.** (2017).
630       Cell Sheet Morphogenesis: Dorsal Closure in *Drosophila melanogaster* as a Model
631       System. *Annu. Rev. Cell Dev. Biol.* **33**, 169–202.

632 **Kumar, A., Rizvi, M. S., Athilingam, T., Parihar, S. S. and Sinha, P.** (2020). Heterophilic
633       cell-cell adhesion of atypical cadherins Fat and Dachsous regulate epithelial cell size
634       dynamics during *Drosophila* thorax morphogenesis. *Mol. Biol. Cell* **31**, 546–560.

635 **Levayer, R., Dupont, C. and Moreno, E.** (2016). Tissue Crowding Induces Caspase-Dependent
636       Competition for Space. *Curr. Biol. CB* **26**, 670–677.

637 **Li, B. and Wang, J. H.-C.** (2011). Fibroblasts and Myofibroblasts in Wound Healing: Force
638       Generation and Measurement. *J. Tissue Viability* **20**, 108–120.

639  **Lin, S.-Z., Li, B., Lan, G. and Feng, X.-Q.** (2017). Activation and synchronization of the
640      oscillatory morphodynamics in multicellular monolayer. *Proc. Natl. Acad. Sci. U. S. A.*
641      **114**, 8157–8162.

642  **Marinari, E., Mehonic, A., Curran, S., Gale, J., Duke, T. and Baum, B.** (2012). Live-cell
643      delamination counterbalances epithelial growth to limit tissue overcrowding. *Nature* **484**,
644      542–545.

645  **Martin, P.** (1997). Wound Healing--Aiming for Perfect Skin Regeneration. *Science* **276**, 75–81.

646  **Martin, P. and Lewis, J.** (1992). Actin cables and epidermal movement in embryonic wound
647      healing. *Nature* **360**, 179–183.

648  **Martín-Blanco, E. and Knust, E.** (2001). Epithelial morphogenesis: filopodia at work. *Curr.*
649      *Biol. CB* **11**, R28-31.

650  **Martín-Blanco, E., Pastor-Pareja, J. C. and García-Bellido, A.** (2000). JNK and
651      decapentaplegic signaling control adhesiveness and cytoskeleton dynamics during thorax
652      closure in *Drosophila*. *Proc. Natl. Acad. Sci. U. S. A.* **97**, 7888–7893.

653  **Molè, M. A., Galea, G. L., Rolo, A., Weberling, A., Nychyk, O., De Castro, S. C., Savery,**
654      **D., Fässler, R., Ybot-González, P., Greene, N. D. E., et al.** (2020). Integrin-Mediated
655      Focal Anchorage Drives Epithelial Zippering during Mouse Neural Tube Closure. *Dev.*
656      *Cell* **52**, 321-334.e6.

657  **Morin, X., Daneman, R., Zavortink, M. and Chia, W.** (2001). A protein trap strategy to detect
658      GFP-tagged proteins expressed from their endogenous loci in *Drosophila*. *Proc. Natl.*
659      *Acad. Sci. U. S. A.* **98**, 15050–15055.

660  **Muliyil, S., Krishnakumar, P. and Narasimha, M.** (2011). Spatial, temporal and molecular
661      hierarchies in the link between death, delamination and dorsal closure. *Development* **138**,
662      3043–3054.

663  **Nagata, S.** (2018). Apoptosis and Clearance of Apoptotic Cells. *Annu. Rev. Immunol.* **36**, 489–
664      517.

665  **Narasimha, M. and Brown, N. H.** (2004). Novel functions for integrins in epithelial
666      morphogenesis. *Curr. Biol. CB* **14**, 381–385.

667  **Narasimha, M., & Brown, N. H.** (2013). Integrins and associated proteins in *Drosophila*
668      development. In *Madame Curie Bioscience Database [Internet]*. Landes Bioscience.

669  **Nikolić, D. L., Boettiger, A. N., Bar-Sagi, D., Carbeck, J. D. and Shvartsman, S. Y.** (2006).
670      Role of boundary conditions in an experimental model of epithelial wound healing. *Am.*
671      *J. Physiol. Cell Physiol.* **291**, C68-75.

672 **Ninov, N., Chiarelli, D. A. and Martín-Blanco, E.** (2007). Extrinsic and intrinsic mechanisms
673     directing epithelial cell sheet replacement during *Drosophila* metamorphosis.
674     *Development* **134**, 367–379.

675 **Norden, C.** (2017). Pseudo-stratified epithelia – cell biology, diversity and roles in organ
676     formation at a glance. *J. Cell Sci.* **130**, 1859–1863.

677 **Parsons, J. T., Horwitz, A. R. and Schwartz, M. A.** (2010). Cell adhesion: integrating
678     cytoskeletal dynamics and cellular tension. *Nat. Rev. Mol. Cell Biol.* **11**, 633–643.

679 **Pasakarnis, L., Frei, E., Caussinus, E., Affolter, M. and Brunner, D.** (2016). Amnioserosa
680     cell constriction but not epidermal actin cable tension autonomously drives dorsal
681     closure. *Nat. Cell Biol.* **18**, 1161–1172.

682 **Pastor-Pareja, J. C., Grawe, F., Martín-Blanco, E. and García-Bellido, A.** (2004). Invasive
683     Cell Behavior during *Drosophila* Imaginal Disc Eversion Is Mediated by the JNK
684     Signaling Cascade. *Dev. Cell* **7**, 387–399.

685 **Prat-Rojo, C., Pouille, P.-A., Buceta, J. and Martin-Blanco, E.** (2020). Mechanical
686     coordination is sufficient to promote tissue replacement during metamorphosis in
687     *Drosophila. EMBO J.* **39**, e103594.

688 **Saias, L., Swoger, J., D'Angelo, A., Hayes, P., Colombelli, J., Sharpe, J., Salbreux, G. and
689     Solon, J.** (2015). Decrease in Cell Volume Generates Contractile Forces Driving Dorsal
690     Closure. *Dev. Cell* **33**, 611–621.

691 **Shaw, T. J. and Martin, P.** (2009). Wound repair at a glance. *J. Cell Sci.* **122**, 3209–3213.

692 **Singh, R., Letai, A. and Sarosiek, K.** (2019). Regulation of apoptosis in health and disease: the
693     balancing act of BCL-2 family proteins. *Nat. Rev. Mol. Cell Biol.* **20**, 175–193.

694 **Sisson, J. C., Field, C., Ventura, R., Royou, A. and Sullivan, W.** (2000). Lava Lamp, a Novel
695     Peripheral Golgi Protein, Is Required for *Drosophila melanogaster* Cellularization. *J.
696     Cell Biol.* **151**, 905–918.

697 **Solon, J., Kaya-Copur, A., Colombelli, J. and Brunner, D.** (2009). Pulsed forces timed by a
698     ratchet-like mechanism drive directed tissue movement during dorsal closure. *Cell* **137**,
699     1331–1342.

700 **Sun, Z., Guo, S. S. and Fässler, R.** (2016). Integrin-mediated mechanotransduction. *J. Cell
701     Biol.* **215**, 445–456.

702 **Suzanne, M. and Steller, H.** (2013). Shaping organisms with apoptosis. *Cell Death Differ.* **20**,
703     669–675.

704 **Teng, X. and Toyama, Y.** (2011). Apoptotic force: Active mechanical function of cell death
705     during morphogenesis. *Dev. Growth Differ.* **53**, 269–276.

706 **Teng, X., Qin, L., Borgne, R. L. and Toyama, Y.** (2017). Remodeling of adhesion and
707    modulation of mechanical tensile forces during apoptosis in *Drosophila* epithelium.
708    *Development* **144**, 95–105.

709 **Toyama, Y., Peralta, X. G., Wells, A. R., Kiehart, D. P. and Edwards, G. S.** (2008).
710    Apoptotic force and tissue dynamics during *Drosophila* embryogenesis. *Science* **321**,
711    1683–1686.

712 **Truman, J. W. and Riddiford, L. M.** (2019). The evolution of insect metamorphosis: a
713    developmental and endocrine view. *Philos. Trans. R. Soc. B Biol. Sci.* **374**, 20190070.

714 **Usui, K. and Simpson, P.** (2000). Cellular Basis of the Dynamic Behavior of the Imaginal
715    Thoracic Discs during *Drosophila* Metamorphosis. *Dev. Biol.* **225**, 13–25.

716 **Vereshchagina, N., Bennett, D., Szöőr, B., Kirchner, J., Gross, S., Vissi, E., White-Cooper,
717    H. and Alphey, L.** (2004). The Essential Role of PP1β in *Drosophila* Is to Regulate Non
718    muscle myosin. *Mol. Biol. Cell* **15**, 4395–4405.

719 **Williams-Masson, E. M., Malik, A. N. and Hardin, J.** (1997). An actin-mediated two-step
720    mechanism is required for ventral enclosure of the C. elegans hypodermis. *Development*
721    **124**, 2889–2901.

722 **Wu, H., Farutin, A., Hu, W.-F., Thiébaud, M., Rafaï, S., Peyla, P., Lai, M.-C. and Misbah,
723    C.** (2016). Amoeboid swimming in a channel. *Soft Matter* **12**, 7470–7484.

724 **Mao, Y., Tournier, A. L., Bates, P. A., Gale, J. E., Tapon, N., & Thompson, B. J.** (2011).
725    Planar polarization of the atypical myosin Dachs orients cell divisions in
726    *Drosophila*. *Genes Dev.*, *25*(2), 131-136.

727 **Yang, J. and Liu, Y.** (2001). Dissection of key events in tubular epithelial to myofibroblast
728    transition and its implications in renal interstitial fibrosis. *Am. J. Pathol.* **159**, 1465–1475.

729 **Young, P. E., Richman, A. M., Ketchum, A. S. and Kiehart, D. P.** (1993). Morphogenesis in
730    *Drosophila* requires non-muscle myosin heavy chain function. *Genes Dev.* **7**, 29–41.

731 **Zeitlinger, J. and Bohmann, D.** (1999). Thorax closure in *Drosophila*: involvement of Fos and
732    the JNK pathway. *Development.* **126**, 3947–3956.

733

734    **Figure legends:**

735    **Figure 1. LEC layer dynamics during thorax closure**

736 **(A-A')** HE and LEC layer during the course of thorax closure: *puc-lacZ* (β-gal, green) mark the

737 leading edge; F-actin (grey), and nuclei (red) (A). (A') Magnified box of (A) reveals

738 lamellipodia (blue arrowhead) and filopodia (red arrowhead). Scale bar: 50 µm.

739 **(B-C)** Snapshots (from left panel of Video 1) for the progression of thorax closure; the edges of

740 HE (green outlined) and LEC layer (red outline) are also shown separately in (C). Scale bar: 100

741 µm.

742 **(D)** Change in surface area of LEC layer before and during the course of thorax closure

743 (quantified from left panel in Video 1) (N=1).

744 **(E)** Increase in the number of nuclei—to predict overcrowding—in the medial region of LEC

745 layer in T2 (Box 1 and 2) segment as compared to T3 segment (Box 3) (see Figure1B for boxes

746 location) (N =2; Mean ± SD).

747 **(F-G)** Tracks of cell movement—as traced from their nuclei (from right panel of Video 1)—in

748 the LEC layer before (0-4 hrs, blue, F) and during (4-6 hrs, green, G) thorax closure.

749 **(H-I)** Cryo-cross sections of T2 segment at 4:30 hrs (H) and 5:30 hrs (I) APF, stained for actin

750 (grey) and LECs (red nucleus) (yellow dotted outlined), the HE (yellow arrows) and

751 delaminating nuclei (yellow star) (N =number or samples tested), Scale bar: 50 µm.

752 **(J-L)** Cell height of3:30 hrs (early) (J) and 5:30 hrs (late) (K) of LEC layer (yellow dotted

753 outline), with delaminated cells (yellow stars); and their respective quantification (L) (N=3 for

754 each of the stages with 10 independent measurements from each sample, Student's t-test,

755 ****p<0.0001, Mean± SEM). Scale bar: 5 µm.

756 (M) Cartoon representation of the dynamic changes in the LEC layer (blue-green)—from a

757 stretched to a crowded state followed by the cell extrusion—parallel to HE migration (brown)

758 during thorax closure.

759 **Figure 2:  Cell delamination and death in LEC layer during thorax closure**

760 **(A)** Snapshots of Lachesin-GFP marked cell outline of LECs (also see Video 2) showing cells

761 undergoing apical constriction (yellow arrowhead) and delamination (red arrowhead) (Scale bar:

762 25 μm).

763 **(B)** Top and X-Z view for controls compared to *p35* overexpression using *A58-Gal4* (also see

764 Figure S1D). Outlines of HE (yellow dotted lines) and LEC layer (white dotted lines and

765 counterstained for actin (red, shown only in lower panel) to mark cell cytoskeleton and muscles.

766 Large masses of LECs shown as (yellow stars) (Scale bar: 50 μm).

767 **(C)** Adult thorax (upper panels) and their respective fluorescent images (lower panels) from the

768 above case (B). Cleft thoraces phenotypes following *p35* overexpression (blue arrowheads in

769 upper panel) and red arrowheads mark persistence of GFP-marked LECs in adults (lower panel)

770 (Scale bar: 200 μm).

771 **(D)** Inter-HE distances in case of *A58>GFP* (control, green) and their respective *p35*

772 overexpression (*A58>GFP; p35*, red) (N=3 for each case, Mean ± SEM, two-way ANOVA was

773 performed, **** p value: <0.0001).

774 **(E)** Cartoon representation of cross-sectional view of the control and those displaying *p35* over-

775 expressions at 6 hrs APF.

776 **Figure 3. Non-muscle myosin II in LEC layer drives thorax closure.**

777 **(A-B)** Time-lapse snapshots of thorax closure in *pnr>GFP* (left panel, Video 4) (A) and

778 following laser ablation (B) (Video 3). Yellow box in (B) represents the region of interest (ROI)

779 for laser ablation. Red star marks the tips of the contralateral HE (Scale bar: A-200 μm and B-50

780 μm).

781 **(C)** Graphical plot to show the increased inter-HE distances following laser ablation (B) during

782 thorax closure.

783 **(D-D''')** Sqh expression in the migrating HE and LEC layer, counterstained with actin (red). The

784 blue boxed area of (D) is magnified (D') to display the patterns of enrichments of Sqh-GFP (D'')

785 and actin (D''') in the LEC layer (Scale bar: 50 μm).

786    **(E-G)** Whole-mounts preparation at 6 hrs APF for control (+, left panel) and their respective *sqh*

787    knockdown (*sqh*-RNAi, right panel) using various Gal4s (see Figure S1B-D); yellow dotted lines

788    represent the edges of HE that failed to zipper (Scale bar: 50 μm).

789    **(H)** Deviation of inter-HE separations at specific time points between control and *sqh*

790    knockdown in E-G (see Video 5 with their respective panels in Video 4) (N =4; Mean ± SEM,

791    ANCOVA test was performed to compare the three linear regression models fits to the 3 cases;

792    ***, p values: <0.001).

793    **Figure 4: Integrin-βPS (Mys) is essential for maintaining HE-LEC contact as well as LEC**

794    **integrity**

795    **(A)** Cartoon representation to check Mys (Integrin βPS1) localization in both the tissues (2 and

796    3) and at the contact points (1, X-Z view) (Scale bar: 50 μm).

797    **(B)** Mys-GFP localization (green) in the HE (magnified further in box 2), LEC (magnified

798    further in box 3) and counterstained for Lgl (red). Broken yellow line marked as 1 to show the

799    X-Z section for LEC-HE contact point and Y-Z view for box 2 and 3 were shown below for Mys

800    localization with respective cartoon representation in (B) (Scale bar: A: 50 μm and Box 2 and 3:

801    25 μm).

802    **(C-E)** Pupal whole mounts stained for actin (red) or nucleus (red): *mys*-knockdown using

803    different Gal4s (see Figure S1B-D). The outlines for HE (cyan) and the LEC (yellow) are shown

804    for their detachment (Scale bar: 50 μm) (also see Video 6).

805    **(F-H)** Eclosed adults at lower temperature from C-E (18□C). Scale bar: 200 μm.

806    **(I)** Deviation of HE separations at specific time points between control and *mys* knockdown (N =

807    4; Mean ± SEM, ANCOVA test was performed to compare the three linear regression models

808    fits to the 3 cases; *** p values: <0.001).

809    **Figure 5: Mathematical modelling of LEC dynamics.**

810    **(A)** Energy functional describing the passive response of the epithelial tissue with contributions

811    from cell elasticity (in red), actomyosin contraction (in blue), and cell-cell adhesion (in cyan).

812    Sqh localization at the cell membrane is considered in the form of active forces (in green).

813    **(B-D)** Three snapshots showing the cell geometries in the initial, intermediate and late stages of

814    thorax closure in wild type scenario. Same snapshots for (C) in the absence of active force,

815    analogous to *sqh-RNAi*, and (D) when the cell delamination is blocked, and (E) when integrin is

816    knockdown.

817

818    **Figure 6: LEC layer generate pull force during thorax closure**

819    Graphical summary of the LEC layer (green) dynamic during thorax closure. LEC layer displays

820    two different force generating mechanisms: a) via virtue of their enriched actomyosin network

821    that allow cells to undergo active contraction (green arrow), and b) crowding induced

822    delamination (rosette yellow cells) (orange arrow), together providing a pull force that drags the

823    above HE to come close at the body midline.

824    Further, LEC layer and HE edge cells are indirectly connected via integrin-based connections

825    (Mys-Scb heterodimer, green), besides LECs displaying integrin-enrichment at the sub-apical

826    junctions, that allow relay of the LECs-forces to the HE tissues and stability to the LEC layer

827    during the contraction phase.

828    **Supplementary Figure Legends:**

829    **Supplementary Figure 1: HE zippering event and the tissue-specific Gal4s used in current**
830    **study**

831    **(A)** Contralateral HEs, undergoing fusion (blue arrow), with LEC layer, marked for actin (grey)

832    at late stages of thorax closure (i.e. 5:00, 5:15, 5:30, and 6:00 hrs APF). Scale Bar: 50 μm.

833    **(B-D)** Domains of expression of *nls*-GFP driven by *pnr-Gal4* (B); *332.3Gal80; pnr-Gal4* (C) and

834    *A58-Gal4* (D). *332.3Gal80* suppresses the expression of *pnr* in LECs. Cartoon represent (column

835    1), actual view in pupae (column 2) and in dissected HE and LEC layer (column 3) with their

836    eclosed adults (column 4) (Scale bars: pupae: 500 µm, tissue mounts: 50 µm and adults: 200

837    µm).

838    **Supplementary Figure 2: LECs shows delamination and early caspase activation**

839    **(A-A')** Whole mount preparation of Spider-GFP marked LECs that shows the presence of

840    delaminating cells—marked by their small apical sizes.

841    **(B)** X-Z view of LECs *(pnr>GFP)* to show delaminated cells (blue arrow) at 5:30 hrs APF.

842    Scale bar: 25 µm.

843    **(C)** Apoliner expression (green nuclei) before (2 hrs APF) and during (4 and 5 hrs APF) thorax

844    closure. Boxed area from each image are shown at a higher magnification in the lower panel

845    (Scale bar: upper panel: 100 µm, lower panel: 50 µm).

846    **(D)** Loss of cells—counted using number of nucleus—in LEC layer (from T2 segment) during

847    the thorax closure (N=2, Mean ± SEM).

848    **Supplementary Figure 3: p35 overexpression spanning LECs impediment the process of**

849    **HE migration and fusion.**

850    **A)** Comparison of the X-Z view for the *pnr-Gal4* driven p35 overexpression (lower panel) with

851    respect to its control (upper panel), counter stained for actin (red).

852    **(B)** Adult thorax (upper panels) and their respective fluorescent images (lower panels) from the

853    above cases. Cleft thoraces phenotypes following *p35* overexpression (blue arrowheads in upper

854    panel) and red arrowheads mark persistence of GFP-marked LECs in adults (lower panel) (Scale

855    bar: 200 µm).

856    **(C)** Inter-HE distances in case of *pnr-Gal4* and their respective *p35* overexpression (N=3 for

857    each case, Mean ± SEM, two-way ANOVA analysis was performed with **** p value:<0.0001).

858    **(D)** Comparison of the X-Z view for the *332.3Gal80; pnr-Gal4* driven p35 overexpression

859    (lower panel) with respect to its control (upper panel), counter stained for actin (red).

860    **Supplementary Figure 4: *scab*, ☐-PS3 integrin, cooperates with *mys* during the process of**

861    **thorax closure**

862    **(A)** Screening for the candidate integrin heterodimer involved during thorax closure. In case of

863    knockdown of βPS1 (*mys)* and αPS3 (*scb)* results in no adults whereas in rest of cases eclosed

864    adults are without any thorax defect. Scale bar: 200µm.

865    **(B-C)** Time-lapse snapshots at different time intervals of thorax closure where αPS3 (*scab*) is

866    knocked down using *pnr-Gal4* (E) and *A58-Gal4* (F) (lower panels) as compared to their

867    respective controls (upper panels). Heminotal position in each case is marked in red star.

868    **Video Legends: (see supplementary information)**

869    **Video 1_Live imaging of LECs and HE:** Left panel showing dual tissue live-imaging during

870    early, mid and late stages of HE migration and finally fusion, whereas, right panel shows the

871    LECs nuclear migration tracks before and during thorax closure.

872    **Video 2_Apical cell constriction and delamination in LEC layer:** Lachesin-GFP marked

873    LECs boundaries showing apical constriction (yellow) and delamination (red).

874    **Video 3_Laser ablation of LEC layer:** *pnr>GFP* staged pupae showing events before and after

875    the laser ablation (red arrow).

876    **Video 4_Domains of Gal4 driver expression**: Controls used for live imaging to understand the

877    process of thorax closure, *pnr>GFP* (left panel), *A58-GFP* (middle panel) and *332.3Gal80;*

878    *pnr>GFP* (right panel) are used in this study.

879    **Video 5_Tissue-specific *sqh* knockdown:** Live imaging of pupae when *sqh* is knockdown using

880    different Gal4 mentioned above: that is, *pnr>GFP; sqh-RNAi* (left panel), *A58-GFP; sqh-RNAi*

881    (middle panel) and *332.3Gal80; pnr>GFP; sqh-RNAi* (right panel).

882    **Video 6_Tissue specific *mys* knockdown:** Live imaging of pupae when *mys* is knockdown

883    using different Gal4 mentioned above: that is, *pnr>GFP; mys-RNAi* (left panel), *A58-GFP; mys-*

884    *RNAi* (middle panel) and *332.3Gal80; pnr>GFP; mys-RNAi* (right panel).

32

885    **Video 7_Mathematical simulation of various LEC parameters during thorax closure:**

886    Visualization of thorax closure when all LEC parameters, identified in this study, are considered

887    (Wild-type, first panel), when non-muscle myosin-II component is absent (second panel), when

888    delamination is absent (third panel), and when integrin adhesions between the two-tissue

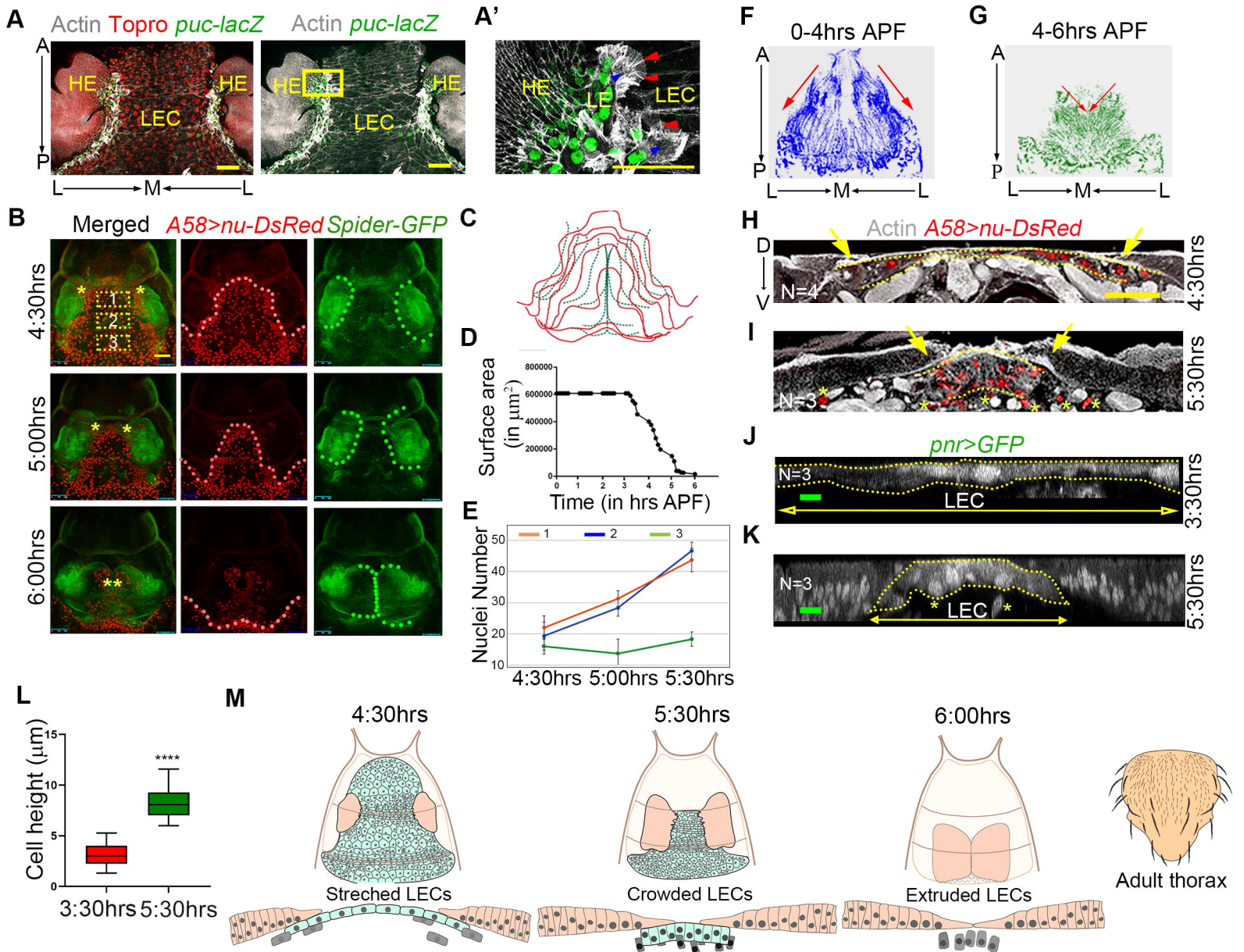889    interface are absent (fourth panel).

# Figure 1

# Figure 2



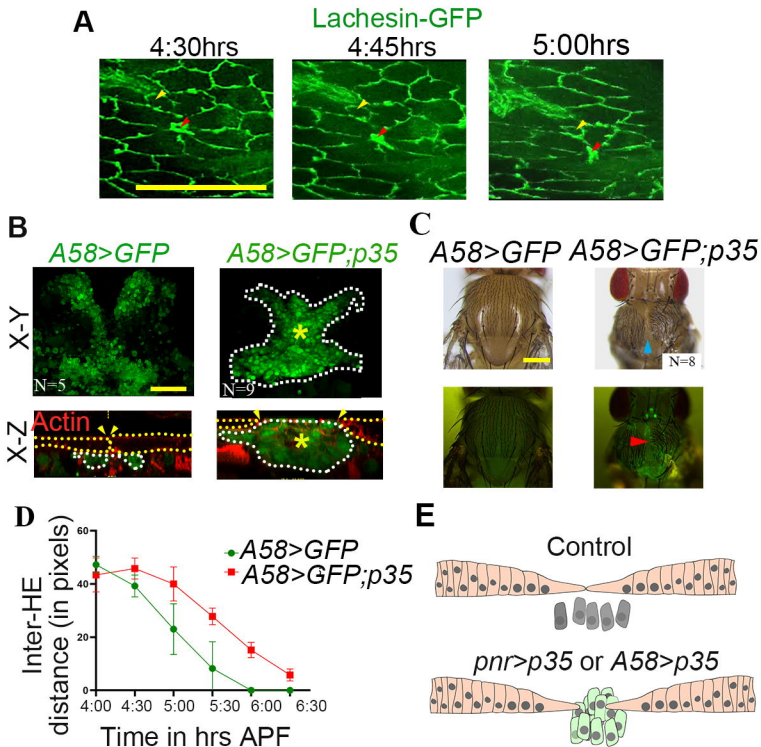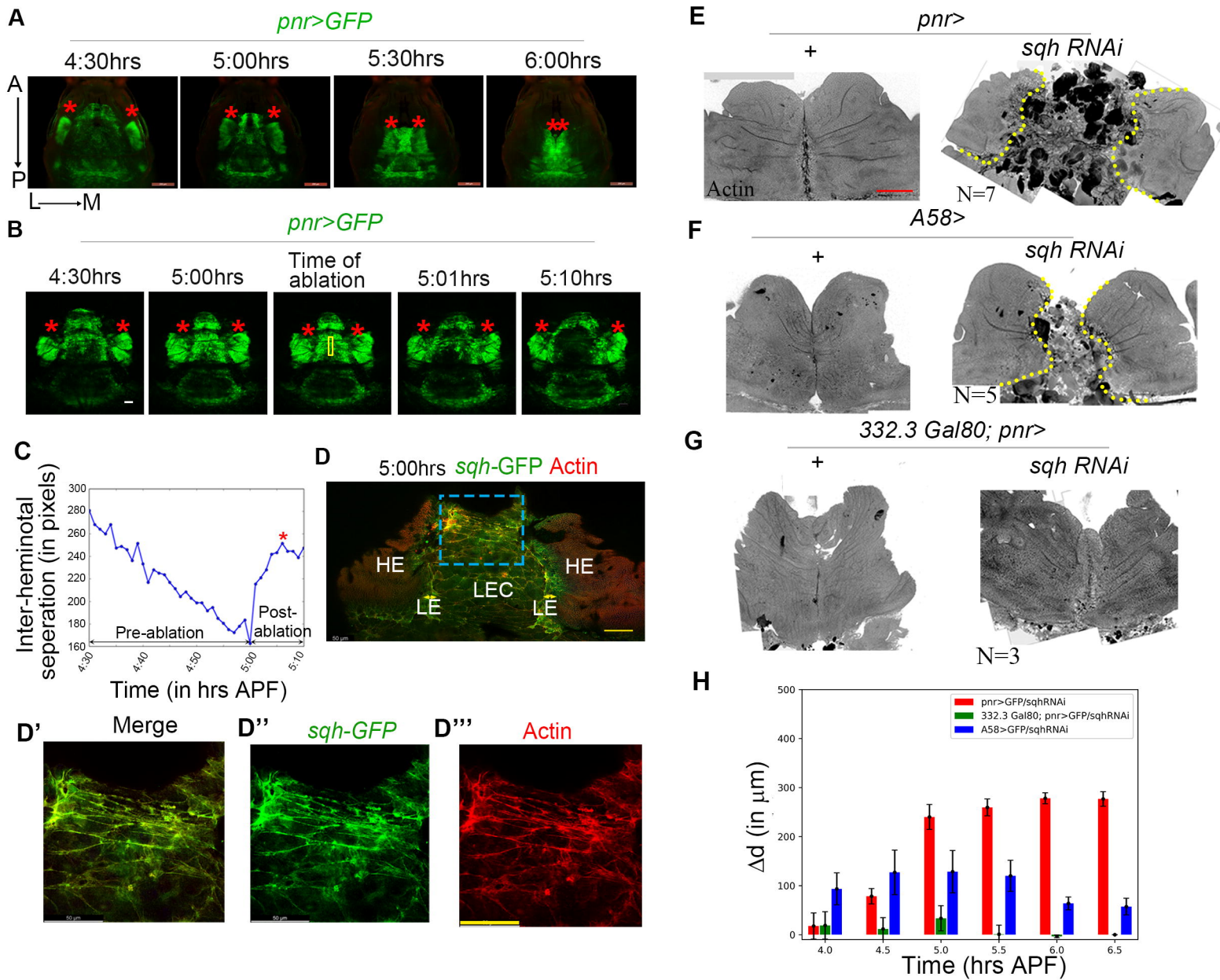**A** Lachesin-GFP
4:30hrs    4:45hrs    5:00hrs

**B**
A58>GFP    A58>GFP;p35
X-Y
N=5    N=9

Actin
X-Z

**C** A58>GFP  A58>GFP;p35
N=8

**D**

Inter-HE distance (in pixels)

● A58>GFP
■ A58>GFP;p35

Time in hrs APF

**E**
Control

pnr>p35 or A58>p35

# Figure 3



**A** *pnr>GFP*

4:30hrs 5:00hrs 5:30hrs 6:00hrs

A
P
L → M

**B** *pnr>GFP*

4:30hrs 5:00hrs Time of ablation 5:01hrs 5:10hrs

**C**

Inter-heminotal seperation (in pixels)

Pre-ablation Post-ablation

Time (in hrs APF)

**D** 5:00hrs *sqh*-GFP Actin

HE HE
LE LEC LE

**D'** Merge **D''** *sqh-GFP* **D'''** Actin

**E** *pnr>*

\+ Actin *sqh RNAi* N=7

**F** *A58>*

\+ *sqh RNAi* N=5

**G** *332.3 Gal80; pnr>*

\+ *sqh RNAi* N=3

**H**

Δd (in μm)

■ pnr>GFP/sqhRNAi
■ 332.3 Gal80; pnr>GFP/sqhRNAi
■ A58>GFP/sqhRNAi

Time (hrs APF)

# Figure 4

**A**

1 — X-Z View
2 — Y-Z view
3 — Y-Z view

Heminota
LEC layer

**B** Mys-GFP  Lgl

1 Y-Z   2 Y-Z
X-Z

HE   LEC

1   HE   LEC

Mys
Lgl

**B'** Box 1

HE

1 (Y-Z)

**B''** Box 2

LEC

2 (Y-Z)

**C** *pnr>GFP; mys RNAi*
Actin

**D** *A58>GFP; mys RNAi*
Nucleus

**E** *332.3; pnr>GFP; mys RNAi*
Actin

**I**

pnr>GFP/mysRNAi
332.3 Gal80; pnr>GFP/mysRNAi
A58>GFP/mysRNAi

Δd (in μm)

Time (hrs APF)

**F** 10/10

**G** N=15/15

**H** N=20/20

# Figure 5

**A**

$$E\left(\mathbf{R}_i\right) = \sum_\alpha \frac{K_\alpha}{2}\left(A - A_\alpha\right)^2 + \sum_\alpha \frac{\Gamma_\alpha}{2} L_\alpha^2 + \sum_{\alpha,\beta} \Lambda_{\alpha\beta} l_{\alpha\beta}$$

$$\mathbf{f}_a(\alpha, \mathbf{R}_i) = g(M(\alpha))\mathbf{n}(\mathbf{R}_i)$$



**B** Wild type

**C** No sqh

**D** No delamination

**E** No Integirn

# Figure 6



LECs Top view

LECs Side view

| | | | |
|---|---|---|---|
| → Apoptotic forces in LECs | ● Squash (sqh) | ▮ Integrins-based adhesion (mys-scb) | ◗ Apoptotic LECs |
| → Actomyosin driven forces in LECs | ✕ Actin | ◖ Delaminating LECs | ▯ Contracting LECs |

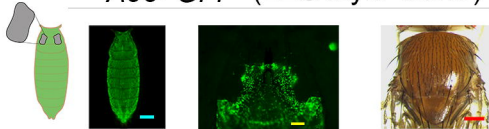# Supplementary Figure 1



**A**

L ⟶ M ⟵ L

A — Actin

P

5:00hrs     5:15hrs     5:30hrs     6:00hrs
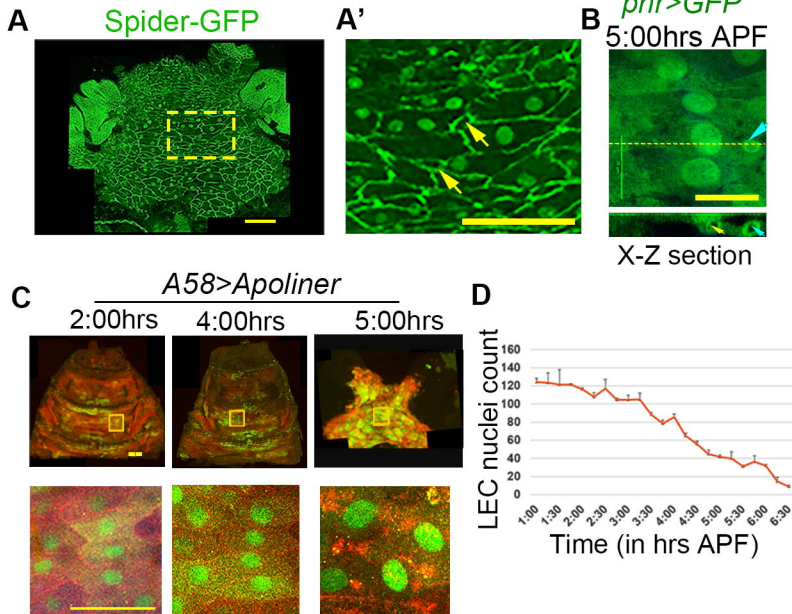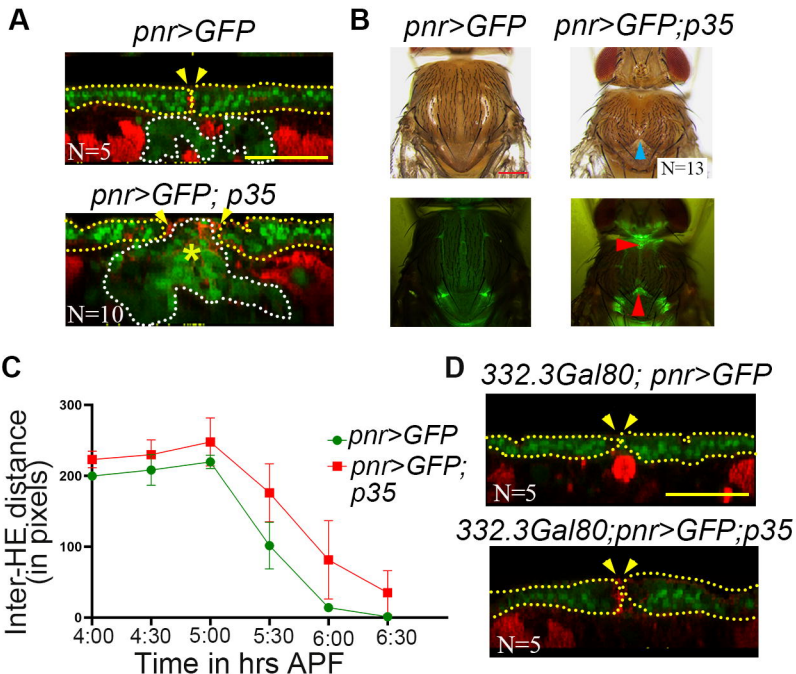
**B** *pnr>GFP* (Both HE and LEC layer driver)
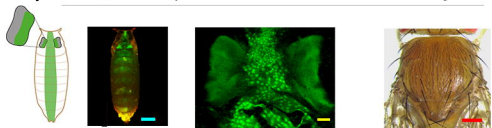
**C** *332.3 Gal80; pnr>GFP* (HE driver)
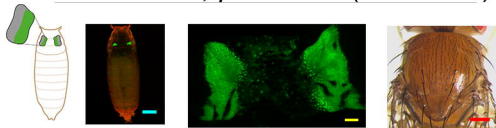
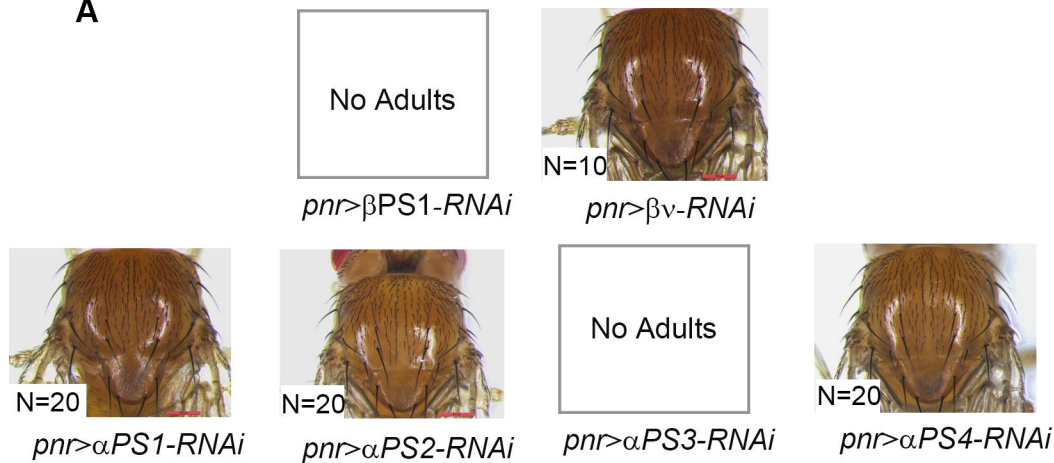**D** *A58>GFP* (LEC layer driver)

# Supplementary Figure 2



**A** Spider-GFP

**A'**

**B** *pnr>GFP*
5:00hrs APF

X-Z section

**C** *A58>Apoliner*

2:00hrs    4:00hrs    5:00hrs

**D**

# Supplementary Figure 3



**A**

*pnr>GFP*

N=5

*pnr>GFP; p35*

N=10

**B**

*pnr>GFP*          *pnr>GFP;p35*

N=13

**C**



Inter-HE distance (in pixels)

300

200

100

0

4:00  4:30  5:00  5:30  6:00  6:30

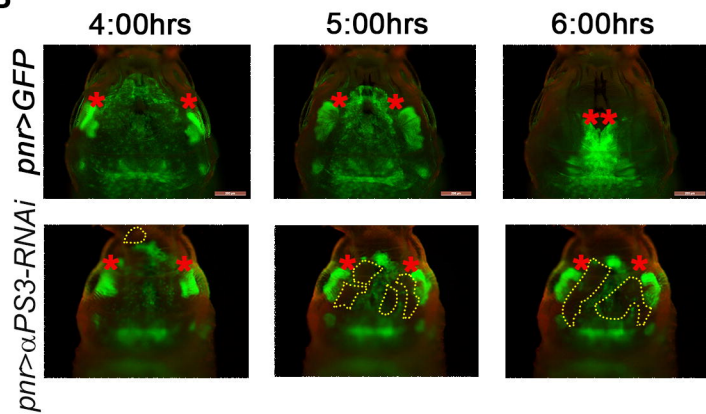Time in hrs APF

● *pnr>GFP*
■ *pnr>GFP; p35*

**D**

*332.3Gal80; pnr>GFP*

N=5

*332.3Gal80;pnr>GFP;p35*

N=5

# Suppplementary Figure 4

**A**



No Adults

*pnr>βPS1-RNAi*

N=10

*pnr>βν-RNAi*

N=20

*pnr>αPS1-RNAi*

N=20

*pnr>αPS2-RNAi*

No Adults

*pnr>αPS3-RNAi*

N=20

*pnr>αPS4-RNAi*

**B**

| | 4:00hrs | 5:00hrs | 6:00hrs |
|---|---|---|---|
| *pnr>GFP* | | | |
| *pnr>αPS3-RNAi* | | | |

**C**

| | 4:00hrs | 5:00hrs | 6:00hrs |
|---|---|---|---|
| *A58>GFP* | | | |
| *A58>αPS3-RNAi* | | | |